Available online at www.sciencedirect.com

SCIENCE DIRECT®

International Journal of Solids and Structures 43 (2006) 5110–5131

INTERNATIONAL JOURNAL OF SOLIDS and STRUCTURES

www.elsevier.com/locate/ijsolstr

The behaviour of a self-piercing riveted connection under quasi-static loading conditions

R. Porcaro [a,*], A.G. Hanssen [b], M. Langseth [a], A. Aalberg [a]

[a] *Structural Impact Laboratory (SIMLab), Department of Structural Engineering, Norwegian University of Science and Technology, N-7491 Trondheim, Norway*
[b] *SINTEF Materials and Chemistry, N-7465 Trondheim, Norway*

Received 15 April 2005; received in revised form 10 August 2005
Available online 13 December 2005

Abstract

The behaviour of a self-piercing riveted connection was investigated experimentally and numerically. An extensive experimental programme was conducted on elementary riveted joints in aluminium alloy AA6060 in two different tempers, T4 and T6. The experimental programme was focused on the influence of important model parameters such as thickness of the plates, geometry of the specimens, material properties of the plates and loading conditions. An accurate 3D numerical model of different types of riveted connections subjected to various loading conditions was generated based on the results of the numerical simulation of the riveting process. A new algorithm was generated in order to transfer all the information from the 2D numerical model of the riveting process to the 3D numerical model of the connection. Thus, the 3D model was initialized with the proper deformed shape and the current post-riveting stress–strain state. The residual stresses and the local changes in material properties due to the riveting process were an important factor in order to get the correct structural behaviour of the model. The simulations have been carried out using the explicit finite element code LS-DYNA. The model was validated against the experimental results in order to get the correct deformation modes and the force–displacement characteristics. The numerical force–displacement curves fitted the experimental ones with reasonable accuracy. Furthermore, the model seemed to be able to describe the correct structural behaviour and thus the failure mechanisms of the self-piercing riveted connections.

Keywords: Self-pierce riveting; Connector; Aluminium; Testing; Modelling

1. Introduction

Self-piercing riveting is widely used in modern car structures. Accurate and reliable modelling of these connections is important for the automotive industry. A better understanding of the mechanical behaviour of the riveted connection is required in order to improve the existing shell-based numerical models of a self-piercing

---

[*] Corresponding author. Tel.: +47 7359 4628; fax: +47 7359 4701.
E-mail address: raffaele.porcaro@ntnu.no (R. Porcaro).

0020-7683/$ - see front matter © 2005 Elsevier Ltd. All rights reserved.
doi:10.1016/j.ijsolstr.2005.10.006

Nomenclature

E	Young's modulus
$\sigma_{0.2}$	true stress at 0.2% plastic strain
σ_{u}	true ultimate stress
σ	true stress
ε	true plastic strain
θ	loading angle
F_x	force normal to the loading direction
F_z	force in the loading direction
N	tensile load
S	shear load
N_{u}	maximum tensile load in pure pull-out condition
S_{u}	maximum shear load in pure shear condition
$F_{z\,\mathrm{max}}$	maximum load
$d_{F\mathrm{max}}$	displacement at maximum load
E_{max}	maximum energy
t	simulation time
u_{max}	maximum displacement applied at the numerical model
t_{max}	termination time
v	velocity
T_1	thickness top plate
T_2	thickness bottom plate
σ_1	material properties top plate
σ_2	material properties bottom plate

riveted connection used in large-scale crash analyses of car structures. The considerable number of variables present in a riveted connection leads to an expensive procedure to completely understand the structural behaviour of such connections by means of experimental procedures. In this context, numerical tools can be used to achieve a better understanding of the physical mechanisms, i.e. failure mechanisms and correct prediction of the strength of the connection.

A literature survey on the behaviour of self-piercing riveted connections found only a limited amount of published data. There have been tests on lap-shear joints using self-piercing rivets and these are compared with other types of connections (Di Lorenzo and Landolfo, 2004; Lennon et al., 1999; Porcaro et al., 2004). Fu and Mallick (2001) have shown the influence of some process parameters on the static strength and fatigue life of self-piercing riveted joints in aluminium alloy. The mechanical behaviour of this type of connection is not only influenced by the geometrical characteristics of the joint, i.e. number and dimensions of the rivets, distance from the edges, thickness of the plates, the process parameters, i.e. die pressure, pre-clamping force and die shape also play a part. Therefore, it is very difficult to predict the strength of a self-piercing riveted connection without experimental tests. There is a lack of analytical description of the strength and hence complete understanding of a joint mechanism leading to failure. Numerical modelling can be a solution for overcoming these problems. However, in order to fully understand the behaviour of this connection, the model should include all the information from the riveting process, i.e. residual stress–strain distribution, plasticity and damage of the materials.

In this paper, the behaviour of self-piercing riveted connections is investigated experimentally and numerically. An extensive experimental programme is conducted using aluminium alloy AA6060 in two different tempers, T4 and T6. The experimental programme is focused on the influence of important model parameters such as thickness and geometry of the specimens, material properties and loading conditions. The influence of such parameter on the response of the connection was presented in term of force–displacement curves and failure modes. The experimental results are used to validate a 3D numerical model of the connections. The 3D FE

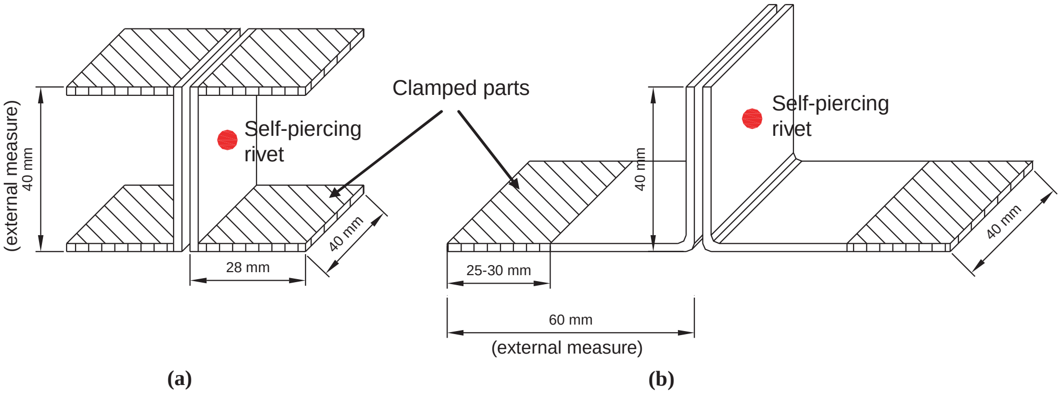

Fig. 1. Geometry of the specimens: (a) U-shaped (single-rivet) specimen, (b) peeling specimen.

representation of this connection is generated using the finite element code LS-DYNA. The model is based on the author's previous results on the simulation of the riveting process (Porcaro et al., in press). A new algorithm is generated in order to map the results from the 2D numerical model of the riveting process to the 3D numerical model of the connection. Thus, the current 3D simulations of the mechanical strength of the riveted joints are initialized with the proper deformed shape and the current post-riveting stress–strain state. Two different specimen geometries are used in this investigation: a U-shaped specimen and a peeling specimen, Fig. 1. The first is composed of two U-shaped aluminium coupons joined with a self-piercing rivet and tested for different loading angles. The second is composed of two L-shaped aluminium coupons joined with a self-piercing rivet. The model is calibrated against the results of a selected specimen. The influence on the model response of important parameters is studied, i.e. loading time, mesh density, element formulation, hourglass control, contact formulation, the initial geometry and the post-riveting initial strain and stress-state. Finally, the capability of the model to reproduce the correct structural behaviour of the connection is discussed in terms of the force–displacement curve and failure modes.

2. Experimental programme

An extensive experimental programme was defined in order to investigate the behaviour of self-piercing riveted connections and to validate a 3D numerical model of such connections. The following model parameters have been used to define the experimental programme: thickness of the plates, strength of the plates and load conditions. The specimens were cut from extrusions of aluminium alloy AA6060 in two different tempers, T4 and T6. Two values for the thickness of the plate were chosen, 2.0 mm and 3.0 mm. A 2^4 factorial design was used in this programme. The selected parameters were: (1) thickness of the top plate, (2) thickness of the bottom plate, (3) material of the top plate and finally (4) material of the bottom plate. The top plate is the plate where the head of the rivet is located. For each combination of these parameters, the rivet geometry and the die shape were chosen in accordance with what is used in the automotive industry today. A listing of the 16 types of specimens with the combination of the different parameters is given in Table 1. Two specimen geometries were used in this investigation: (1) U-shaped specimens, (2) peeling specimen. The U-shaped specimens were tested under three different loading angles (i.e. $\theta = 0°$ pure shear, $\theta = 45°$ and $\theta = 90°$ pure pull-out). As three repetitions were conducted for all the tests, there were 192 tests in this experimental programme, 144 (U-shaped) + 48 (peeling) (Table 2).

3. Material properties

Material tests were carried out in order to characterize the material properties of the specimen and the rivet. The material properties of the aluminium alloy were obtained by means of uniaxial tensile tests. Three samples were cut along the extrusion direction and Fig. 2(a) shows the typical stress–strain curves for the two tempers.

Table 1
Definition of the specimens

Configuration	ID specimen		Thickness		Material		Rivet[a]	Die[a]
	U-shaped	Peeling	Plate 1 (mm)	Plate 2 (mm)	Plate 1	Plate 2		
c1	s1	p1	2	2	AA6060 T4	AA6060 T4	C 5 × 6	DZ 090 2025
c2	s2	p2	2	2	AA6060 T6	AA6060 T6	C 5 × 6	FM 100 2018
c3	s3	p3	2	2	AA6060 T4	AA6060 T6	C 5 × 6	DZ 090 2025
c4	s4	p4	2	2	AA6060 T6	AA6060 T4	C 5 × 6	DZ 090 2025
c5	s5	p5	2	3	AA6060 T4	AA6060 T4	C 5 × 6.5	FM 110 2017
c6	s6	p6	2	3	AA6060 T6	AA6060 T6	C 5 × 6.5	FM 110 2017
c7	s7	p7	2	3	AA6060 T4	AA6060 T6	C 5 × 6.5	FM 110 2017
c8	s8	p8	2	3	AA6060 T6	AA6060 T4	C 5 × 6.5	FM 110 2017
c9	s9	p9	3	2	AA6060 T4	AA6060 T4	C 5 × 6.5	FM 110 2017
c10	s10	p10	3	2	AA6060 T6	AA6060 T6	C 5 × 6.5	FM 110 2017
c11	s11	p11	3	2	AA6060 T4	AA6060 T6	C 5 × 6.5	DZ 090 2025
c12	s12	p12	3	2	AA6060 T6	AA6060 T4	K 5 × 7	FM 110 2017
c13	s13	p13	3	3	AA6060 T4	AA6060 T4	K 5 × 8	FM 120 2019
c14	s14	p14	3	3	AA6060 T6	AA6060 T6	K 5 × 8	FM 120 2019
c15	s15	p15	3	3	AA6060 T4	AA6060 T6	K 5 × 8	FM 120 2019
c16	s16	p16	3	3	AA6060 T6	AA6060 T4	K 5 × 8	FM 120 2019

[a] Böllhoff rivet and die identification. Plate 1 (top plate) is the plate where the head of the rivet is located.

Table 2
Test programme

Specimen geometry	Design	Model parameters						Repetition	Number of tests
		Levels	T_1 (mm)	T_2 (mm)	σ_1	σ_2	θ		
U-shaped	2 × 2 × 2 × 2 × 3	1	2	2	T4	T4	0	3	144
		2	3	3	T6	T6	45		
		3					90		
Peeling	2 × 2 × 2 × 2	1	2	2	T4	T4		3	48
		2	3	3	T6	T6			

T_1 = thickness of Plate 1, T_2 = thickness of Plate 2, σ_1 = material Plate 1, σ_2 = material Plate 2, θ = loading angle.

The material properties of the rivet, which was made of high-strength steel, were provided by the producer of the rivets (Bollhoff). In order to check the mechanical properties of the rivet, a cylinder was cut from the shank of the rivets and tested in lateral compression. A numerical model of this cylinder was generated using hexahedral solid elements, with a mesh size of 0.1 mm × 0.1 mm × 0.1 mm, that corresponds with the mesh size that

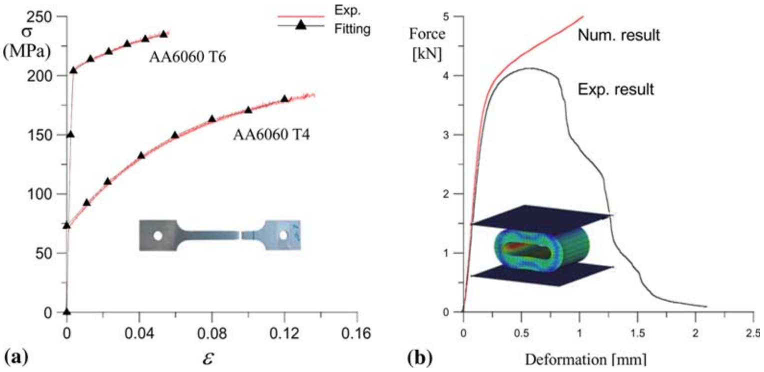

Fig. 2. Material characterization: (a) aluminium material, (b) rivet material.

Table 3
Material parameters

Material	Young's modulus, *E* (MPa)	Yield stress, $\sigma_{0.2}$ (MPa)	Ultimate stress, σ_u (MPa)
T4	69,911	73.0	180.0
T6	67,068	150.1	234.0
Rivet	188,000	1520.0	–

was used for the rivet in the model of the riveting process. The material of the rivet and the aluminium alloy were modelled as an elasto-plastic material, adopting the von Mises yield criterion, an isotropic linear strain-hardening rule and the associated flow rule in the plastic domain (*MAT_PIECEWISE_LINEAR_PLASTICITY), type 24 in LS-DYNA. Fig. 2(b) shows the comparison between the model and the experimental results. In the numerical model of the cylinder, failure was not included. The experimental force–displacement curve starts to drop due to failure, whereas the numerical curve continues to rise. This difference is not important in this study, since in the riveting process the plastic strains in the rivet are less than those causing failure in the cylinder. Table 3 lists Young's modulus E, the true stress at 0.2% plastic strain $\sigma_{0.2}$ and the true ultimate stress σ_u.

4. Experimental test set-up

Two specimen geometries were tested: (a) U-shaped specimen and (b) peeling specimen. The U-shaped specimen is composed of two U-shaped elements joined together in the central part with one rivet, Fig. 1(a). The rivet is the Böllhoff type and is made of high-strength steel with a nominal diameter of 5.0 mm. The peeling specimen is composed of two L-shaped elements. The small flanges were joined with one rivet while the long flange is clamped into the testing machine, Fig. 1(b).

The U-shaped specimens were tested under different loading combinations in the test set-up presented by Porcaro et al. (2004). This test fixture enables to mix and control tensile and shear loads. The angular position between the centreline of the specimens and load application line exactly defines the tensile/shear load ratio of the specimen. The test fixture was designed so that these two straight lines intersect at the centre of the rivet. Fig. 3 shows the test fixture with a loading angle of 45°. Varying the angular position leads to several load combinations. The system of the pull bars and the test fixture surrounding the test specimen can be regarded as a rigid system. Hence, the external work done on the test specimen can only be carried out in the direction

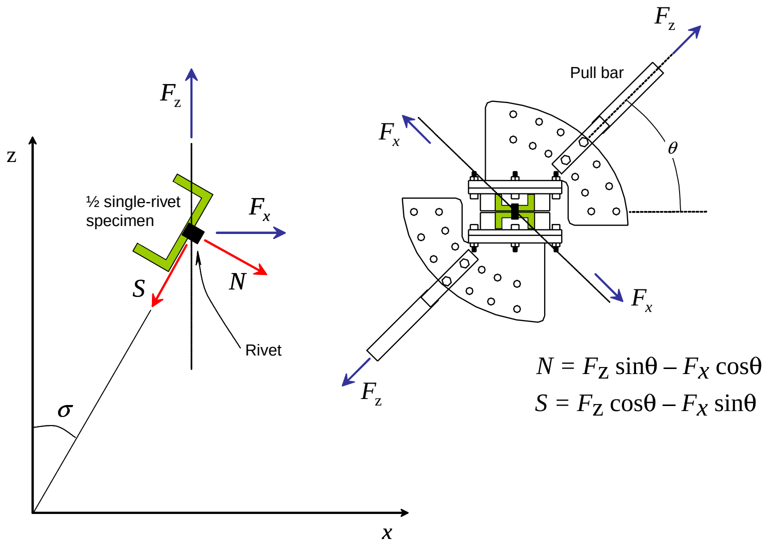

Fig. 3. Schematic of the test fixture.

of the loading defined by the angle θ. No work can be carried out normal to this loading direction since the displacement is zero. However, a force F_x is generally needed in this direction to satisfy the requirements of zero displacements. The loads F_z and F_x may be resolved into two components (tensile load N and shear load S) as a function of the angular position θ

$$N(\theta) = F_z \cdot \sin(\theta) - F_x \cdot \cos(\theta) \tag{1}$$

$$S(\theta) = F_z \cdot \cos(\theta) + F_x \cdot \sin(\theta) \tag{2}$$

This experimental set-up was developed to study the behaviour of a self-piercing riveted joint for pure quasi-static loading conditions. The experimental results obtained with this test fixture were used to obtain an engineering failure criterion in the form

$$\left(\frac{N}{N_{\mathrm{u}}}\right)^a + \left(\frac{S}{S_{\mathrm{u}}}\right)^b = 1 \tag{3}$$

Here, the normal force N and the tensile force S were normalized with respect to the maximum normal force N_{u} when $\theta = 90°$ (pure tension) and the maximum tensile force S_{u} when $\theta = 0°$ (pure shear). Based on the results present by Porcaro et al. (2004) and the number of variables considered in this study, only three angular positions (0°, 45° and 90°) were tested in order to describe the total behaviour of the connection.

The test fixture was connected with an Instron tension–torsion machine by fixing the pull bar into the clamping device of the machine. The tests were performed under displacement control, with a rate of displacement of approximately 3.4×10^{-2} mm/s. The load–displacement histories were recorded during testing and the displacement measured from the machine is representative of the displacement of the test specimen. Tests were terminated when the two components in the specimens were completely separated.

The peeling specimens were tested in a Dartec tension machine with a load cell of 25 kN under displacement control, with a rate of displacement of approximately 20 mm/s. The specimens were clamped to the machine using mechanical grips. The load–displacement histories were recorded during testing as the displacement of the crosshead of the testing machine.

5. Experimental results and failure modes

The results are given in terms of loading angle θ, maximum load $F_{z\max}$, displacement at maximum load $d_{F\max}$ and failure mode for all the specimens, see Tables 4 and 5. Three parallel tests were carried out for each load angle θ and the average values are reported in the tables. The maximum loads were obtained from the load–displacement curves of the tests.

Fig. 4 shows typical load–displacement curves for the U-shaped specimen (Fig. 1(a)). The behaviour of the joint is a function of the combination of the different parameters (thicknesses of the plates and material properties of the plates) as well as the loading angle. Fig. 4(a) and (b) show the load displacement curves for different loading angles respectively for the specimen types "s2" and "s14". The maximum load as well as the initial stiffness decreased with increasing loading angle. This was observed for all the specimens. Otherwise, the displacement at failure increased as the loading angle increased for the specimens with a plate thickness of 2 mm (Fig. 4(a) and (b)). Fig. 4(c) and (d) respectively show the influence of the thickness of the plates and the material properties of the plates on the behaviour of the joint under a pure shear condition.

Fig. 5 presents typical load–displacement curves for the peeling specimen (Fig. 1(b)). The behaviour of the peeling specimens is similar to the behaviour of the U-shaped specimen under the pure pull-out condition. The maximum force is a function of the strength of the plate (Fig. 5(a)) as well as the thickness of the plates (Fig. 5(b)). The maximum force grew when the thickness and the strength of the plates increased. The maximum force as well as the displacement at failure was more dependent on the bottom plate than the top plate. The maximum force decreased if the bottom plate was weaker than the top plate.

Typical failure modes for the U-shaped specimen together with the corresponding force–displacement curves are given in Figs. 6–12. With regard to shear loading, three failure modes were observed:

Failure mode Fs1: Tilting and pull-out of the rivet from the bottom plate. The rivet rotated generating yield and fracture in the material of the top plate while it is sliding out from the bottom plate, Fig. 6.

Table 4
Experimental results

Specimen ID	Loading angle	U-shaped and peeling specimens					
		$F_{z\,\max}$ (kN)		$d_{F\max}$ (mm)		Failure modes	
		Tests	Simulations	Tests	Simulations	Tests	Simulations
s1	0	4.91	4.24	2.89	4.13	Fs1	Fs1
s1	45	3.07	3.22	5.14	1.61	Fs1 + Fs4	Fs1 + Fs4
s1	90	2.53	1.85	7.27	4.43	Fs4	Fs4
p1		1.22	0.83	22.63	9.24	Fp1	Fp1
s2	0	7.19	6.89	2.37	3.60	Fs1	Fs1
s2	45	4.33	5.12	4.35	2.02	Fs1 + Fs4	Fs1 + Fs4
s2	90	3.65	3.52	6.48	4.66	Fs4	Fs4
p2		1.80	1.71	22.79	13.09	Fp1	Fp1
s3	0	5.96	5.64	2.71	2.78	Fs1	Fs1
s3	45	3.77	4.31	4.96	2.67	Fs1 + Fs4	Fs1 + Fs4
s3	90	3.31	3.30	7.88	6.72	Fs4	Fs4
p3		1.55	1.57	20.98	17.10	Fp2	*Fp1*
s4	0	6.00	5.76	2.62	3.49	Fs1	Fs1
s4	45	3.30	4.14	4.61	2.75	Fs1 + Fs4	Fs1 + Fs4
s4	90	2.38	1.88	5.63	3.56	Fs4	Fs4
p4		1.20	0.94	14.13	8.53	Fp1	Fp1
s5	0	6.69	5.37	2.66	3.94	Fs2	Fs2
s5	45	3.89	4.07	4.08	3.40	Fs2 + Fs5	Fs2 + Fs5
s5	90	3.66	3.33	6.22	6.19	Fs5	*Fs4*
p5		1.56	1.95	17.20	20.62	Fp2	*Fp1*
s6	0	9.14	8.18	2.97	2.79	Fs2	Fs2
s6	45	5.12	5.61	3.67	2.82	Fs2 + Fs5	Fs2 + Fs5
s6	90	4.66	5.22	4.99	5.48	Fs5	Fs5
p6		2.15	2.47	15.86	19.32	Fp2	Fp2
s7	0	6.30	6.34	3.26	4.09	Fs2	Fs2
s7	45	3.63	4.52	4.46	4.96	Fs2 + Fs5	Fs2 + Fs5
s7	90	3.45	3.70	5.78	5.47	Fs5	Fs5
p7		1.72	1.86	17.55	15.99	Fp2	Fp2
s8	0	7.75	6.80	2.69	3.60	Fs2	Fs2
s8	45	4.76	4.99	3.95	3.03	Fs2 + Fs5	Fs2 + Fs5
s8	90	4.37	3.36	6.68	4.13	Fs5	*Fs4*
p8		1.72	1.78	18.79	11.52	Fp2	*Fp1*

Failure mode Fs2: Tilting and pull-out of the rivet head from the top plate. The rivet is stuck in the bottom plate while being rotated and going out from the top plate dragging the material under the head of the rivet, Fig. 7.

Failure mode Fs3: Shearing of the bottom plate. The rivet is stuck in the top plate and shearing takes place in the bottom plate, Fig. 8.

Tilting and pull-out of the rivet is the predominant failure mode in the current investigation. All the specimens with the same thickness for the top and the bottom plates have shown this failure mode. The shearing of the bottom plate was observed only for the two specimens of type s9 and s12. In both cases the thicker plate (3 mm) was connected to the thinner one (2 mm) and the latter was made of the weakest material (AA6060 T4). The specimens with the thinner plate as the top plate, i.e. type s5–s6–s7–s8, developed failure type Fs2.

With regard to tension loading two failure modes were observed:

Failure mode Fs4: Pull-out of the rivet from the bottom plate takes place. The rivet is going out from the bottom plate dragging material from the bottom part in contact with the shank of the rivet. This failure mode is always followed by the bending of the plate, Fig. 9.

Failure mode Fs5: Pull-over of the sheeting. The rivet goes out from the top plate dragging the material under the rivet head, Fig. 10. This failure mode only occurs when the top plate is the thinner one and for specimen type s15. Here the bottom and the top plates have the same thickness, but different material properties. The bottom plate is in temper T6 and has thus higher strength than the top plate.

Table 5
Experimental results

Specimen ID	Loading angle	U-shaped and peeling specimens					
		$F_{z\max}$ (kN)		$d_{F\max}$ (mm)		Failure modes	
		Tests	Simulations	Tests	Simulations	Tests	Simulations
s9	0	6.17	5.79	6.57	4.13	Fs3	*Fs1*
s9	45	2.93	3.86	2.99	1.43	Fs1 + Fs4	Fs1 + Fs4
s9	90	1.97	1.47	3.16	1.24	Fs4	Fs4
p9		1.04	0.64	12.31	2.19	Fp1	Fp1
s10	0	7.55	7.96	4.11	3.60	Fs1	Fs1
s10	45	3.71	4.44	1.66	0.91	Fs1 + Fs4	Fs1 + Fs4
s10	90	2.91	1.92	2.93	0.69	Fs4	Fs4
p10		1.68	0.79	8.86	1.80	Fp1	Fp1
s11	0	5.95	7.01	3.21	3.86	Fs1	Fs1
s11	45	3.90	4.95	2.61	2.19	Fs1 + Fs4	Fs1 + Fs4
s11	90	2.78	2.99	3.72	2.91	Fs4	Fs4
p11		1.58	1.44	11.57	7.39	Fp1	Fp1
s12	0	8.07	10.36	6.24	5.31	Fs3	*Fs1*
s12	45	3.77	6.01	3.16	3.88	Fs1 + Fs4	Fs1 + Fs4
s12	90	2.62	1.55	3.93	1.79	Fs4	Fs4
p12		1.17	0.79	11.61	4.97	Fp1	Fp1
s13	0	7.87	7.77	3.07	4.83	Fs1	Fs1
s13	45	5.31	5.61	4.57	3.63	Fs1 + Fs4	Fs1 + Fs4
s13	90	4.54	3.81	6.09	4.01	Fs4	Fs4
p13		2.35	1.97	18.65	11.56	Fp1	Fp1
s14	0	9.84	11.43	3.13	5.66	Fs1	Fs1
s14	45	6.92	8.04	3.23	2.82	Fs1 + Fs4	Fs1 + Fs4
s14	90	5.85	6.46	5.11	2.88	Fs4	Fs4
p14		3.22	3.28	18.48	10.47	Fp1	Fp1
s15	0	8.49	8.27	3.38	4.78	Fs1	Fs1
s15	45	5.78	5.51	4.51	4.09	Fs1 + Fs5	Fs2 + Fs5
s15	90	5.30	6.05	6.11	5.58	Fs5	*Fs4*
p15		2.77	3.36	15.86	18.75	Fp2	Fp2
s16	0	9.20	11.05	3.72	5.96	Fs1	Fs1
s16	45	5.85	7.08	3.55	4.01	Fs1 + Fs4	Fs1 + Fs4
s16	90	4.80	3.81	5.12	3.62	Fs4	Fs4
p16		2.63	1.97	13.55	7.36	Fp1	Fp1

Finally the failure modes of the specimens subjected to a combination of shear and tensile load, i.e. 45°, can be explained as a combination of the previous failure modes, Figs. 11 and 12.

For all the load combinations, the deformation of the rivet appeared to be elastic.

With regard to the peeling connections two failure modes were observed:

Failure mode Fp1: Pull-out of the rivet from the bottom plate. This failure mode is always followed by bending of the plate, Fig. 13.

Failure mode Fp2: Pull-over of the sheeting. In this case, the deformation is concentrated in the top plate (the soft part of the connection) while the bottom plate is rigid, Fig. 14.

6. Numerical model

In a self-piercing riveted connection, the region around the rivet is a very complex zone due to the riveting process where the actual material properties vary from point to point. In a large-scale crash simulation of a shell-based structure, these details (stress–strain distribution in the region around the rivet) are normally ignored and the whole zone is replaced by a single element, i.e. a rigid beam, a non-linear spring or a solid element, which represents the homogeneous behaviour of the region. In order to understand the influence of these parameters, i.e. stress–strain distribution and final geometrical configuration of the joint, a 3D model was generated based on the results from the riveting process simulation performed with LS-DYNA (Hallquist,

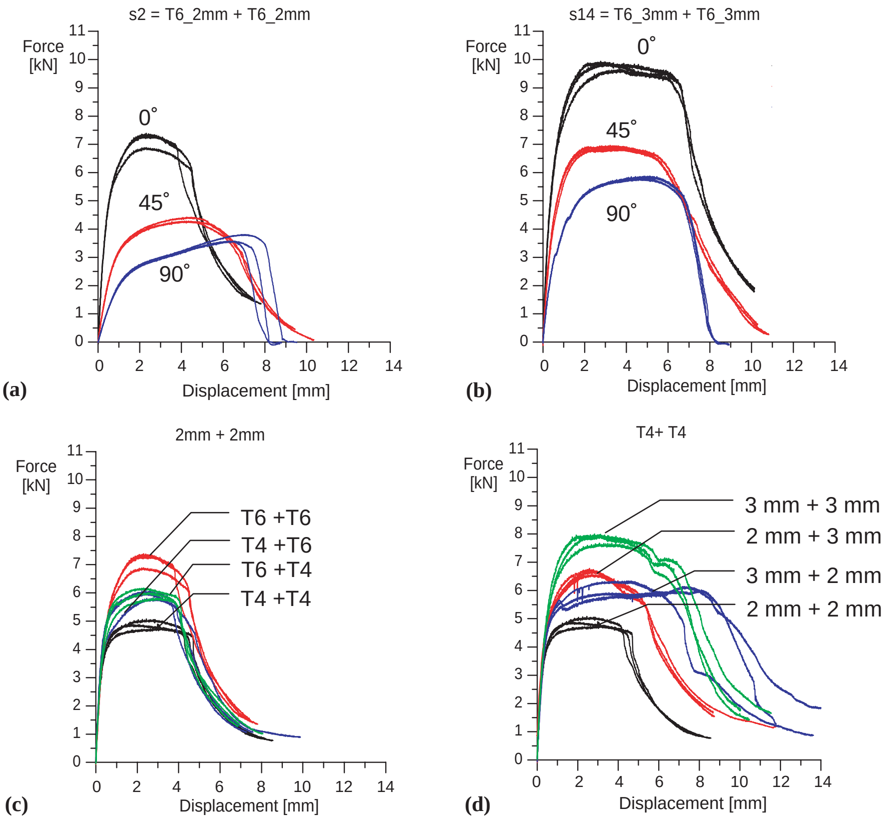

Fig. 4. Representative experimental force–displacement curves for U-shaped specimens: (a) specimen s2 under different loading angles; (b) specimen s14 under different loading angles; (c) pure shear condition ($\theta = 0°$) for specimens s1, s2, s3 and s4; (d) pure shear condition ($\theta = 0°$) for specimens s1, s5, s9 and s13.

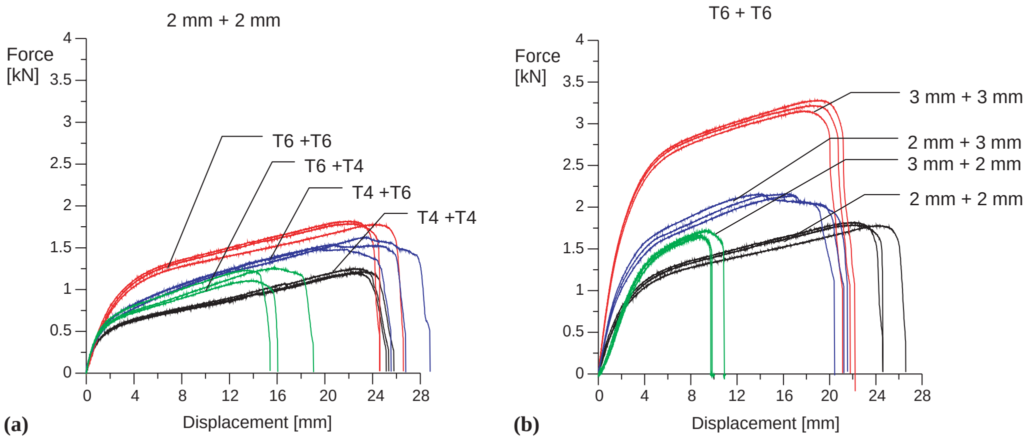

Fig. 5. Representative experimental force–displacement curves for peeling specimens: (a) peeling specimens p1, p2, p3 and p4; (b) peeling specimens p2, p6, p10 and p14.

1998; Livermore Software, 2003). The 3D model is divided into two sub-groups: the internal part and the external part, Fig. 15. The first part is representative of the region that contains the rivet, Fig. 15(a). It is composed of the top plate, the bottom plate and the rivet. The geometry and the material properties are obtained from the riveting process simulation. The region of interest, where the material properties have changed due to

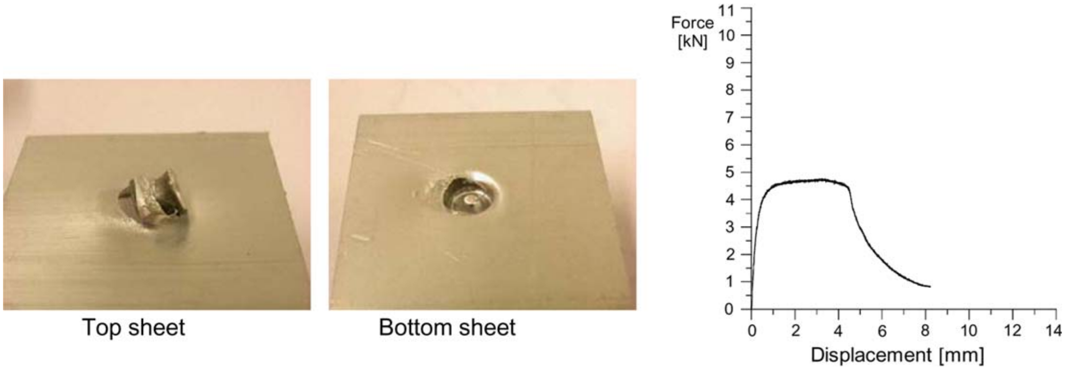
Top sheet
Bottom sheet

Fig. 6. Left: Failure mode Fs1 for specimen s1 (T4_2 mm + T4_2 mm). Right: force–displacement curve.

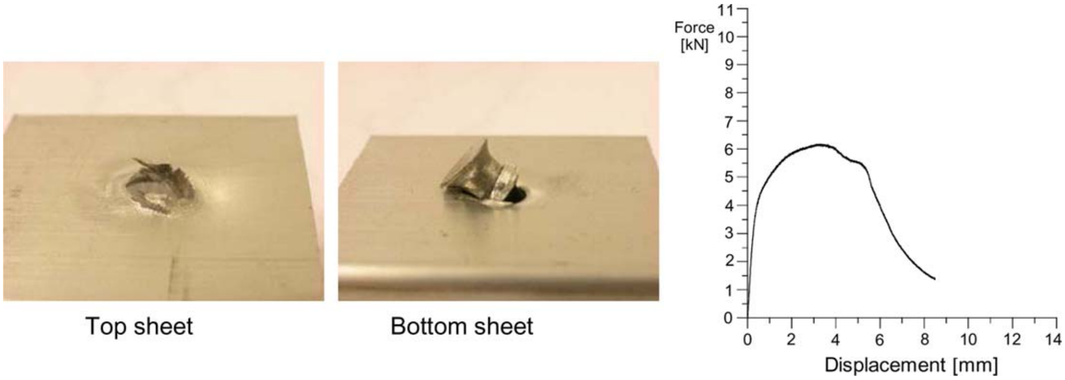
Top sheet
Bottom sheet

Fig. 7. Left: Failure mode Fs2 for specimen s6 (T4_2 mm + T6_3 mm). Right: force–displacement curve.

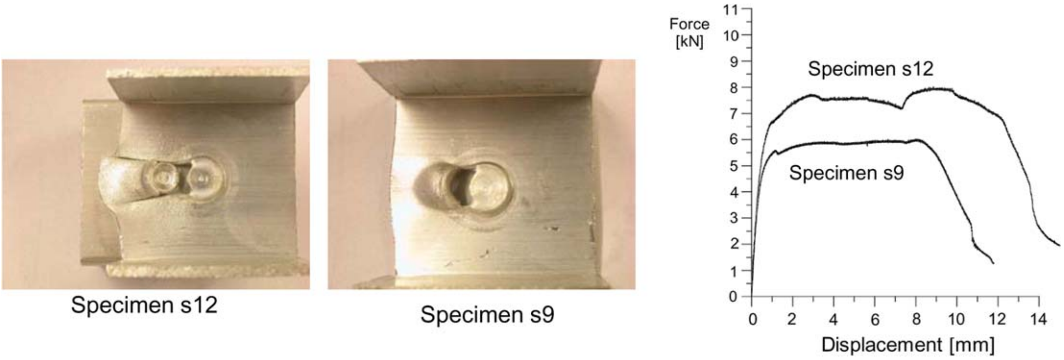
Specimen s12
Specimen s9

Fig. 8. Left: Failure mode Fs3 for specimen s9 (T4_3 mm + T4_2 mm) and s12 (T6_3 mm + T4_2 mm). Right: force–displacement curve.

the riveting process, is the region around the rivet inside the die and blank holder region. The diameter of this region is equal to 24 mm. Outside this region no changes in material properties have been observed in the riveting process simulation. The second part is the rest of the geometry of the specimen (U-specimen or peeling specimen) with a hole in the middle where the internal part is then inserted, Fig. 15(b) and (c). The material properties for the last part correspond to the ‘‘virgin’’ material obtained from tensile tests.

The riveting process simulations (Porcaro et al., in press) were performed using 4-node 2D axisymmetric elements, as the problem is axisymmetric, with four integration points. The size of the smallest element was 0.1×0.1 mm^2, Fig. 16(a). The simulation was ended with the generation of a file containing the geometry

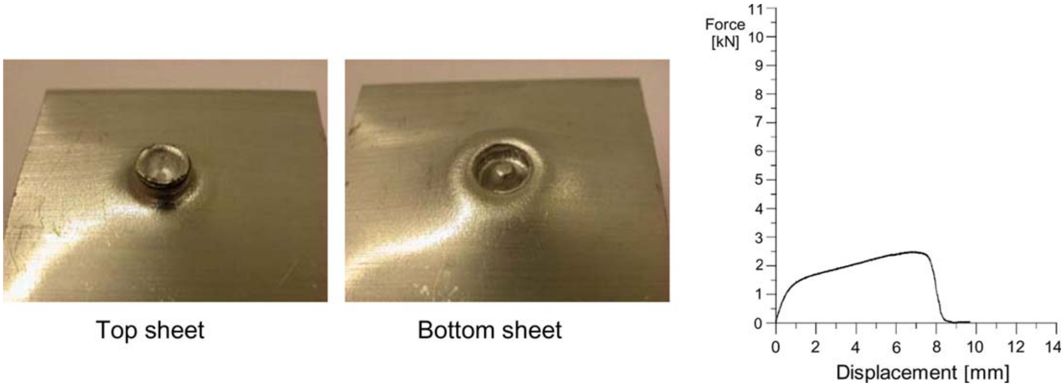

Fig. 9. Left: Failure mode Fs4 for specimen s1 (T4_2 mm + T4_2 mm). Right: force–displacement curve.

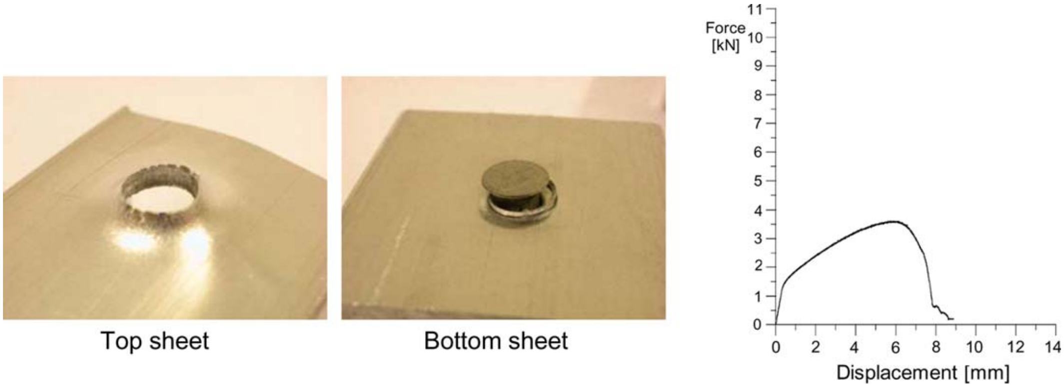

Fig. 10. Left: Failure mode Fs5 for specimen s5 (T4_2 mm + T4_3 mm). Right: force–displacement curve.

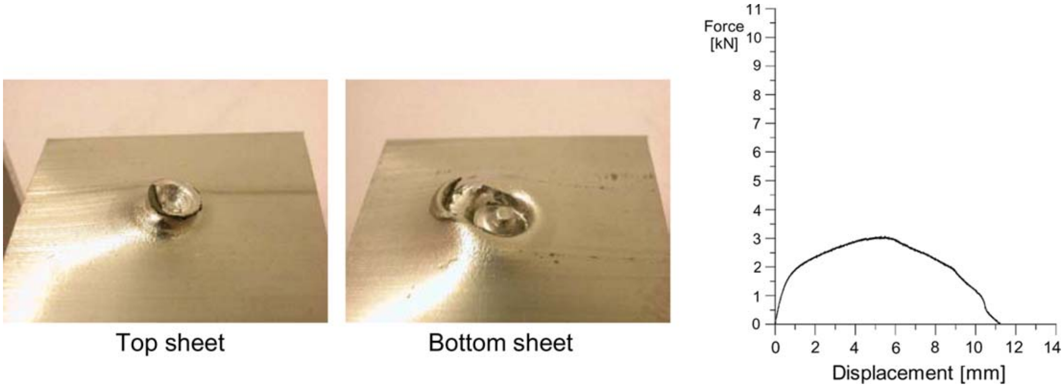

Fig. 11. Left: Failure mode Fs1+Fs4 for specimen s1 (T4_2 mm + T4_2 mm). Right: force–displacement curve.

and material properties of the final configuration of the joint. This file has been used as a starting point to create the mesh of the internal part, Fig. 16(c). LS-DYNA does not present any subroutine able to map data from a 2D simulation to a 3D model. A new algorithm was created in order to generate the internal part. The mesh of the internal part was generated in two steps. In the first step, the old mesh (Fig. 16(a)) was deleted while keeping the border of each part. A new coarser mesh was generated for each part (Fig. 16(b)), finer in the central part along the contact interfaces between the rivet and the plates and coarser in the region

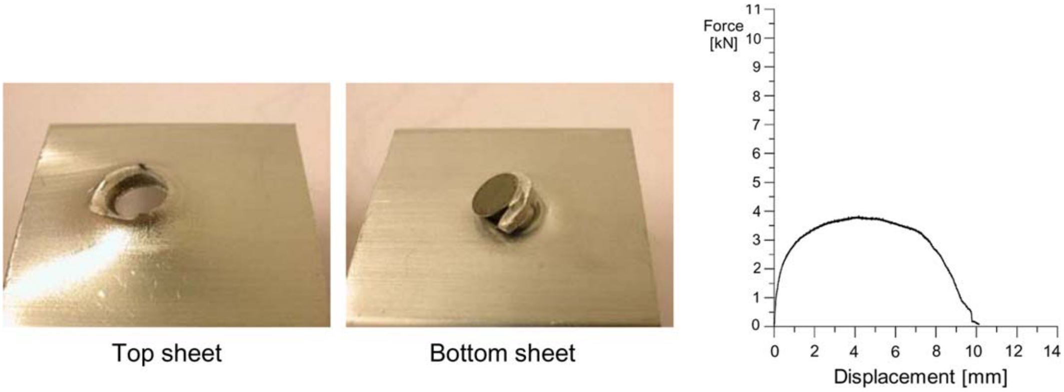

Fig. 12. Left: Failure mode Fs2+Fs5 for specimen s5 (T4_2 mm + T4_3 mm). Right: Force–displacement.

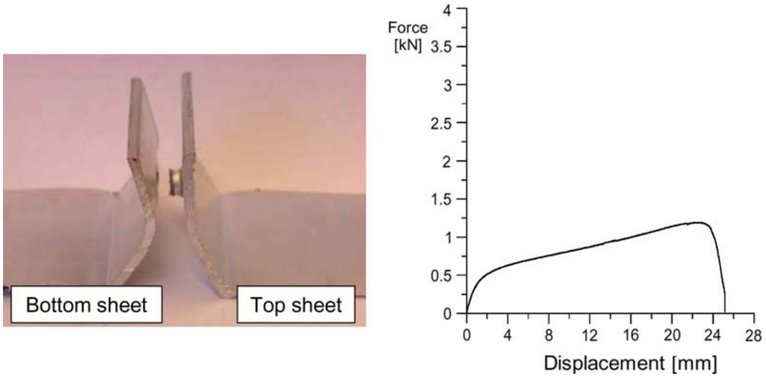

Fig. 13. Left: Failure mode Fp1 for specimen p1 (T4_2 mm + T4_2 mm). Right: force–displacement curve.

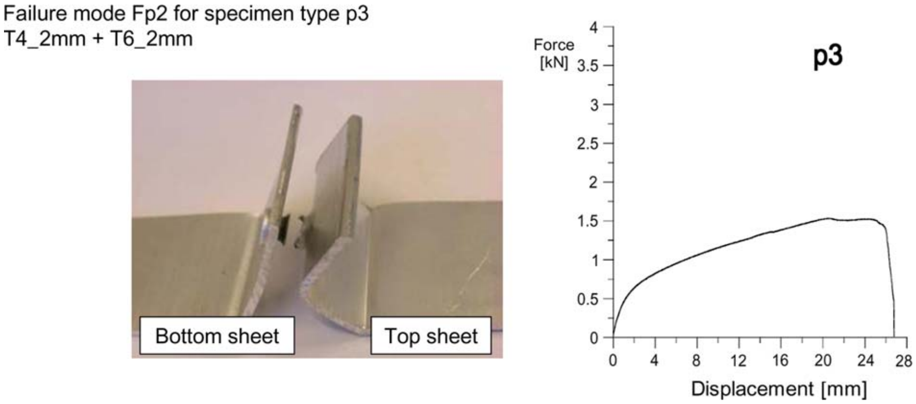

Fig. 14. Left: Failure mode Fp2 for specimen p3 (T4_2 mm + T6_2 mm). Right: Force–displacement curve.

far from the centre. Every part was revolved around the axes of symmetry. Care was taken in the region close to the axes of symmetry in order to avoid wedge shaped elements, Fig. 16(d). In the second step, the stress–strain field was mapped. For each element in the final configuration of the riveting process, the stress–strain field was reduced from four integration points up to one point located in the middle of the element. The average value of the four integration points was applied at this point, Fig. 17(a). Considering the new coarser mesh, the value of the initial stress at the one integration point in the element is the average value of all

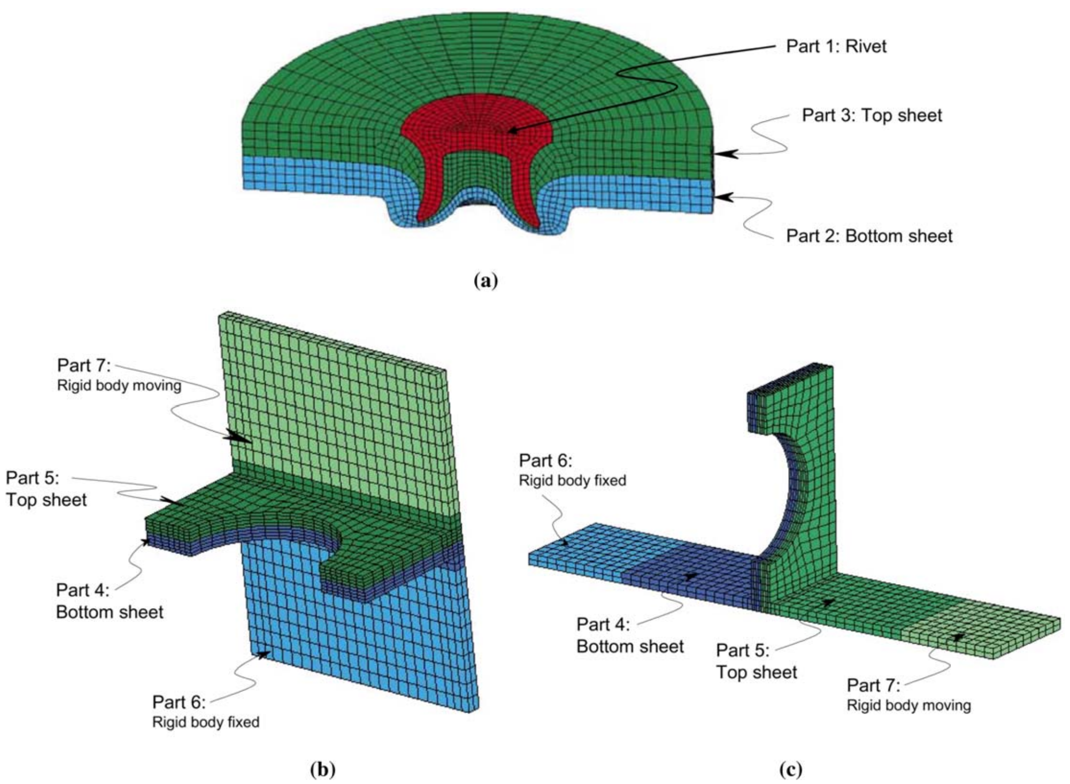

(a)

(b)

(c)

Fig. 15. Geometry of the numerical model: (a) Internal part, (b) U-specimen, (c) Peeling specimen.

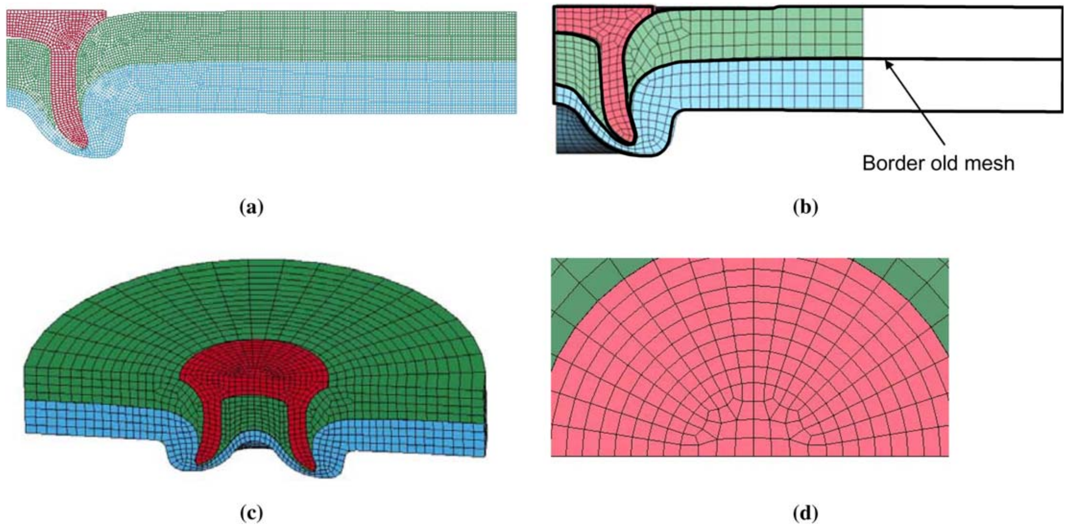

(a)

(b)

(c)

(d)

Fig. 16. Generation of the internal part: (a) Riveting process, (b) New coarser mesh, (c) 3D model of new mesh and (d) close-up of the central part.

the points that are located inside this element, Fig. 17(c). The same value was then applied to all the elements located on the same circumference, Fig. 17(d). The internal part was then merged with the external part. The external mesh was generated such that the number of nodes and elements along the interface were the same as in the internal part. The two parts were thus merged together by replacing the duplicate nodes on the interface

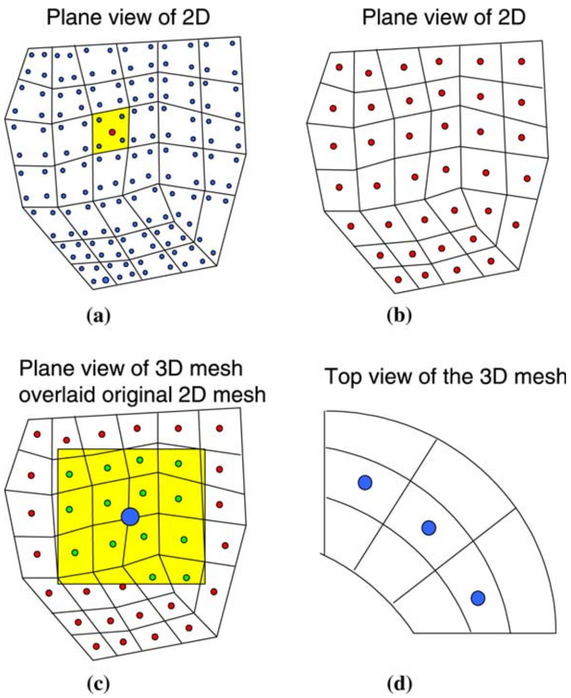

Fig. 17. Mapping of the history variables: (a) four integration points for each element (●), (b) average value are mapped to integration point of 2D element (●), (c) average value are mapped to integration point of 3D element (●); (d) integration point of 3D element with the same radius (●).

surface with only one node. In order to simplify the model, only half of the specimen was modelled using symmetry conditions. The material of the rivet and the aluminium alloy were modelled as an isotropic elasto-plastic material (*MAT_PIECEWISE_LINEAR_PLASTICITY), type 24 in LS-DYNA, Fig. 2. No failure criterion was specified in the material model.

7. Robustness study

In order to calibrate the numerical model, one specimen configuration has been selected: s7 (rivet: diameter = 5 mm, length = 6.5 mm; top plate: thickness = 2 mm, material = AA6060 T4; bottom plate: thickness = 3 mm and material = AA6060 T6). The model presents a mesh distribution denoted m1 as follows (Fig. 18): in the thickness direction the mesh size goes from $0.3 \times 0.3\ \mathrm{mm}^2$ in the central region of the internal part (rivet and part of the plate in contact with the rivet) to $0.5 \times 0.5\ \mathrm{mm}^2$ (4 elements through the thickness in the top plate and 6 in the bottom plate) in the external region of the internal part. In order to merge the internal and external parts, the number of elements through the thickness was equal; in the circumferential direction there were 20 elements. The mesh is finer in the central part in order to improve the contact between the rivet and the plates reducing penetration problems. On the other side, the mesh is coarser towards the boundary in order to reduce the computational time, which is affected both by the element size and number.

The mesh for the 3D model was generated using 8-node hexahedron solid elements. Three simulations were performed with different element formulations, i.e. 1-point integration with constant stress ‘‘ef1’’, selective reduced integrated element (constant pressure) ‘‘ef2’’, and fully integrated (8-node element with nodal rotation) ‘‘ef3’’. Hourglass control is needed for the 1-point integration element to avoid artificial deformation modes (zero energy modes). Three hourglass controls were used, i.e. Flanagan–Belytschko viscous form with exact volume integration (type 3 in LS-DYNA), Flanagan–Belytschko stiffness form with exact volume integration (type 5), Belytschko–Bindeman assumed strain co-rotational stiffness form (type 6). The results are presented in terms of force–displacement curves. As shown in Fig. 19, the simulation with the fully integrated

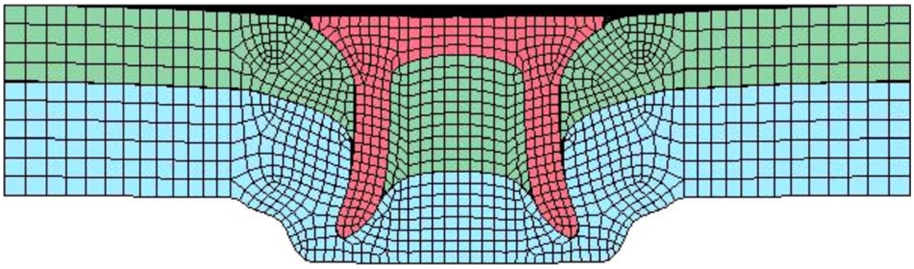

Fig. 18. Section view of the internal part for specimen s7 with the mesh configuration m1.

element, ef3, gives the best fit with the experimental curves. In this case, the simulation time is approximately ten times higher compared with a simulation with one-point integration elements. Considering the simulation with one-point integration elements and changing the hourglass control, we can have the same results as with the fully integrated element using the hourglass control type 6 with an hourglass coefficient of 0.5.

Quasi-static analyses were performed using an explicit time integrator algorithm. When static problems are solved as a dynamic event using explicit codes, it is very important to choose the time scale in an optimal way. The necessary solution time should be as short as possible for computational efficiency, but at the same time sufficiently long enough to ensure that the structure undergoes the correct quasi-static deformation mode. The load was applied with a prescribed velocity as follows:

$$v(t) = \frac{u_{\max} \cdot \pi}{(\pi - 2) \cdot t_{\max}} \left(1 - \cos\left(\frac{\pi \cdot t}{2 \cdot t_{\max}}\right)\right) \tag{4}$$

Here, $u_{\max}$ is the maximum displacement applied and $t_{\max}$ is the termination time.

The influence of loading-time was examined with respect to the predicted load–displacement curves. In order to determine a suitable loading time, four analyses with loading time $t = 1, 2.5, 5, 10$ ms were performed for the specimen geometry with a loading angle of 0° (pure shear). As shown in Fig. 20, the solution converges for a value of the termination time greater than 2.5 ms.

The influence of the mesh density, through the thickness and in the circumferential direction, on the behaviour of the model has been studied. Four configurations were simulated, i.e. m1 (presented earlier), m2, m3 and m4. In the configuration m2 the mesh size through the thickness in the internal part is 0.2×0.2 mm^2, equivalent to 10 elements in the top plate and 15 elements in the bottom plate. In the configuration m3 the mesh size through the thickness in the internal part is 0.1×0.1 mm^2, equivalent to 20 elements in the top plate and 30 in the bottom plate. In the circumferential direction configurations m2 and m3 present the same number of elements as configuration m1. In configuration m4 the mesh density through the thickness is equal to configuration m1, while the number of elements in the circumferential direction is 40. The results are presented in terms of force–displacement curves and simulation time, Fig. 21. As shown in Fig. 21(a), the mesh density

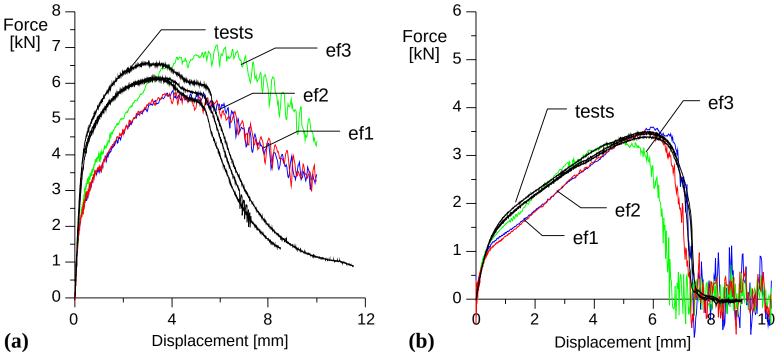

Fig. 19. Force–displacement curve for different element formulation: (a) pure shear, (b) pure pull-out.

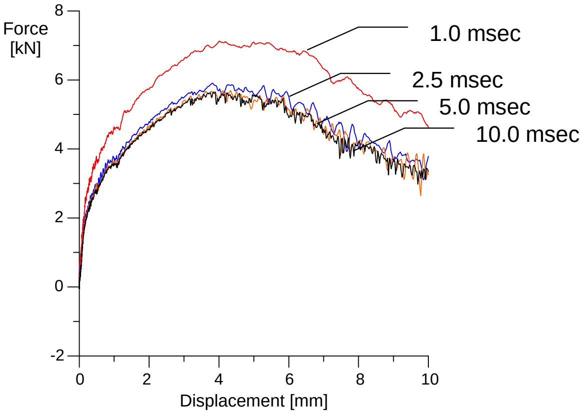

Fig. 20. Influence of the termination time.

does not seem to affect the response of the model. However, the simulation time increases reducing the element size, Fig. 21(b). When increasing the number of elements in the circumferential direction, some oscillations were observed for m4.

Finally, the influence of the initial configuration based on the 2D-model was studied in terms of initial geometry and post-riveting stress–strain distribution. In order to understand the influence of the initial geometry, a process simulation was performed changing the friction between the rivet and the plates in order to achieve a different configuration. Fig. 22 shows the initial geometries of the new configuration m5 compared with the configuration m1 mentioned above. Due to the higher coefficient of friction between the rivet and the top plate, the rivet is cutting through the top plate dragging material of the top plate with the rivet shank. Thus, in configuration m5 the rivet shank is not directly in contact with the bottom plate, a thin layer of material from the top plate is present between the rivet shank and the bottom plate, and there is a gap between the rivet head and the top plate, Fig. 22(b). The response of the model is influenced from the results of the 2D riveting process simulations in terms of force displacement curve, as is clearly shown in Fig. 23(a), and the failure modes. In the case of pure pull-out, configuration m1 has shown a failure mode Fs5 as observed in the experiments, while in configuration m5, the failure mode Fs4 was achieved which is in contrast with the experiments. Furthermore, a simulation was performed without mapping the post-riveting stress–strain distribution. When the post-riveting stress–strain distribution is not mapped a lower force is observed in the model, Fig. 23(b).

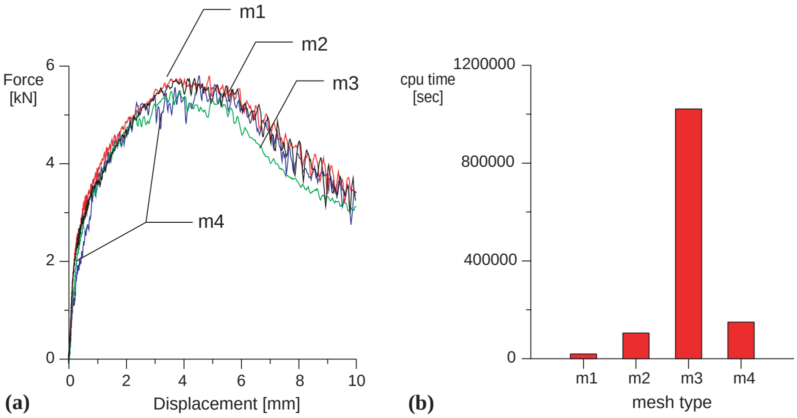

Fig. 21. Influence of the mesh density: (a) force–displacement curve, (b) simulation time.

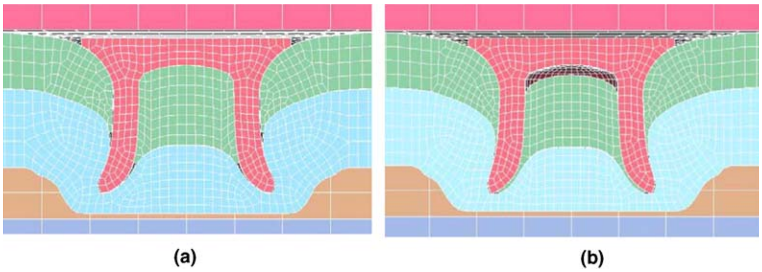

Fig. 22. Initial configuration based on the 2D model: (a) configuration m1, (b) configuration m5.

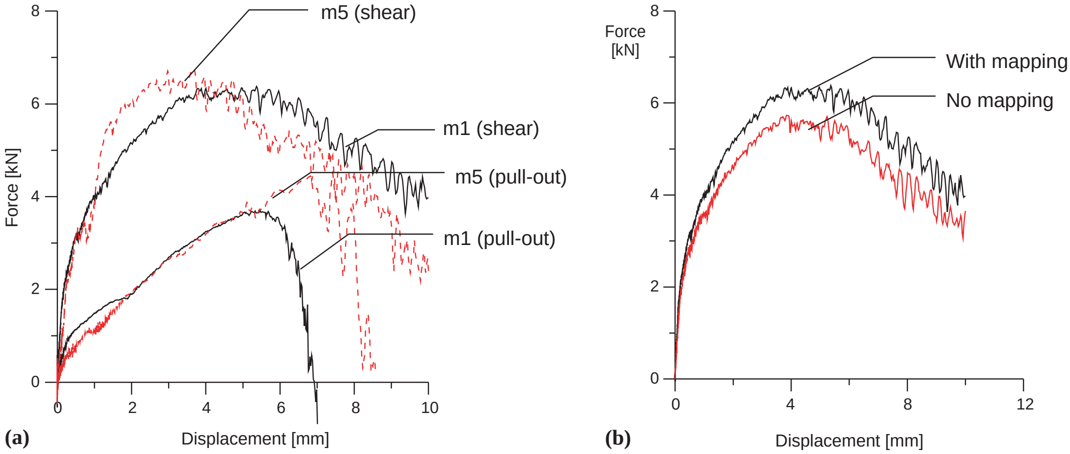

Fig. 23. Influence for the initial configuration based on the 2D model: (a) initial geometry, (b) Post riveting stress–strain distribution.

8. Numerical results and comparison with tests

Based on the robustness study, the following model was used in the comparison with the tests. The mesh in the thickness direction was $0.25 \times 0.25\ \text{mm}^2$ in the central region of the internal part, the rivet and the region of the plates in contact with the rivet. As we move far from the central part, the mesh became coarser, i.e. $0.5 \times 0.5\ \text{mm}^2$. In the external part the number of elements is kept equal to the internal part, in order to be able to merge the two parts. In the circumferential direction, there are 20 elements. The termination time was 3.0 ms and the 8-node hexahedral element with 1-point integration and constant stress was used together with a stiffened-based hourglass control (assumed strain co-rotational stiffness form). The hourglass coefficient was set to 0.5. Furthermore, a pinball segment-based contact algorithm was used with the following values for the friction between the different parts: 0.2 between the rivet and the plates and 0.15 between the plates. The load was prescribed at the flange of the upper plate, while the flange of the bottom plate was fixed. The flanges were defined as rigid bodies.

Results from the simulations are compared with the experimental results in Tables 4 and 5, in terms of maximum force in the loading direction, $F_{z\max}$, displacement at the maximum force, $d_{F\max}$ and failure mode.

Figs. 24 and 25 show the comparison between the numerical and the experimental force–displacement curves. As shown in the figures, the model is able to reproduce the measured curves with reasonable accuracy. In some cases, as for specimen type s6, Table 4, the model is able to predict the correct force–displacement curve as well as the failure model for all the loading conditions. For the specimen type s9 and s10, the model is not able to reproduce the correct force–displacement curve for the pull-out condition, due to assumed incorrect initial geometry, i.e. the rivet has not penetrated enough into the bottom plate resulting in a limited opening of the rivet shank. This has affected the results of the pull-out simulation, but has not influenced the results for the other two loading conditions. In some cases the model over-predicts the force level, because the model

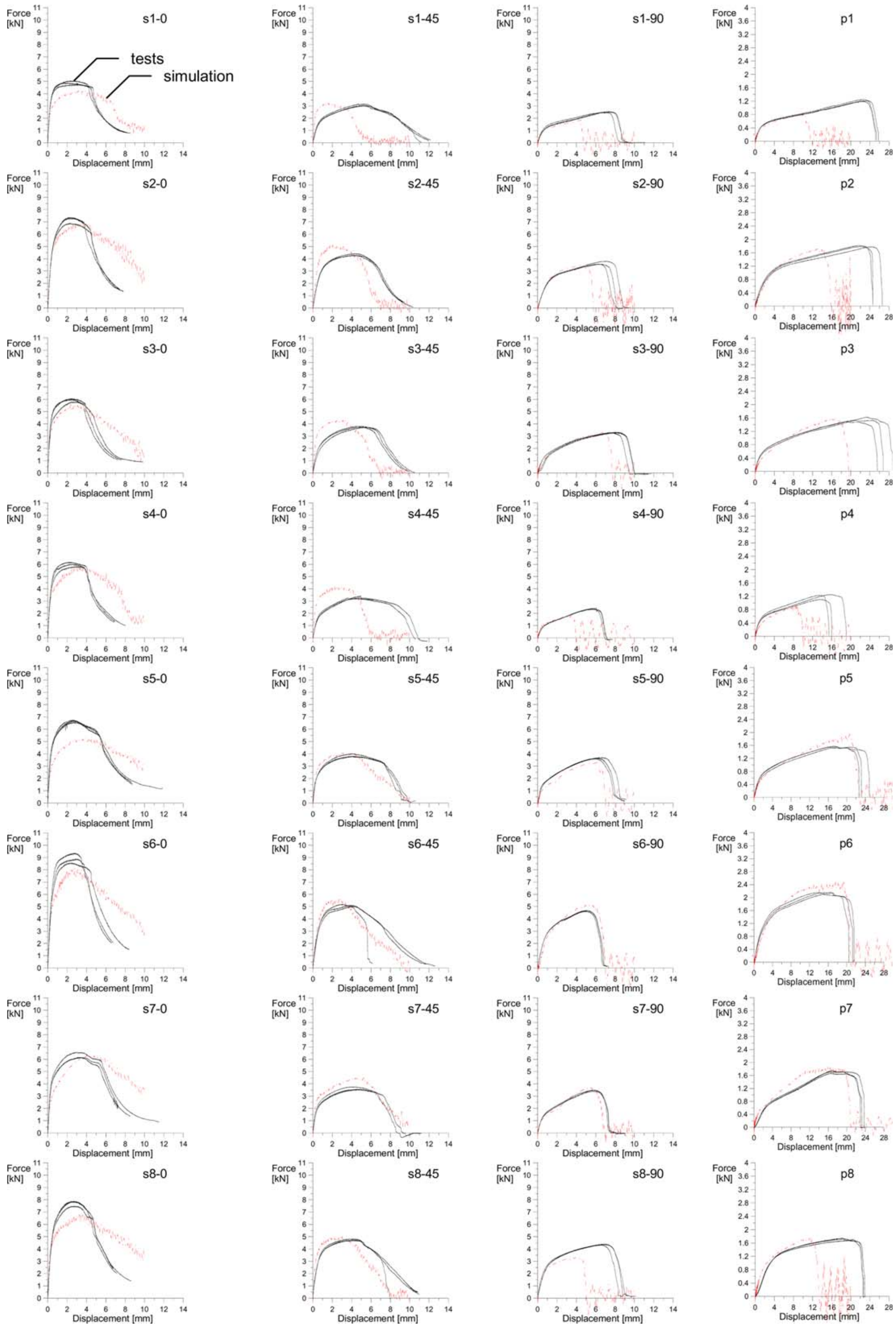

Fig. 24. Comparison between numerical and experimental force–displacement curves.

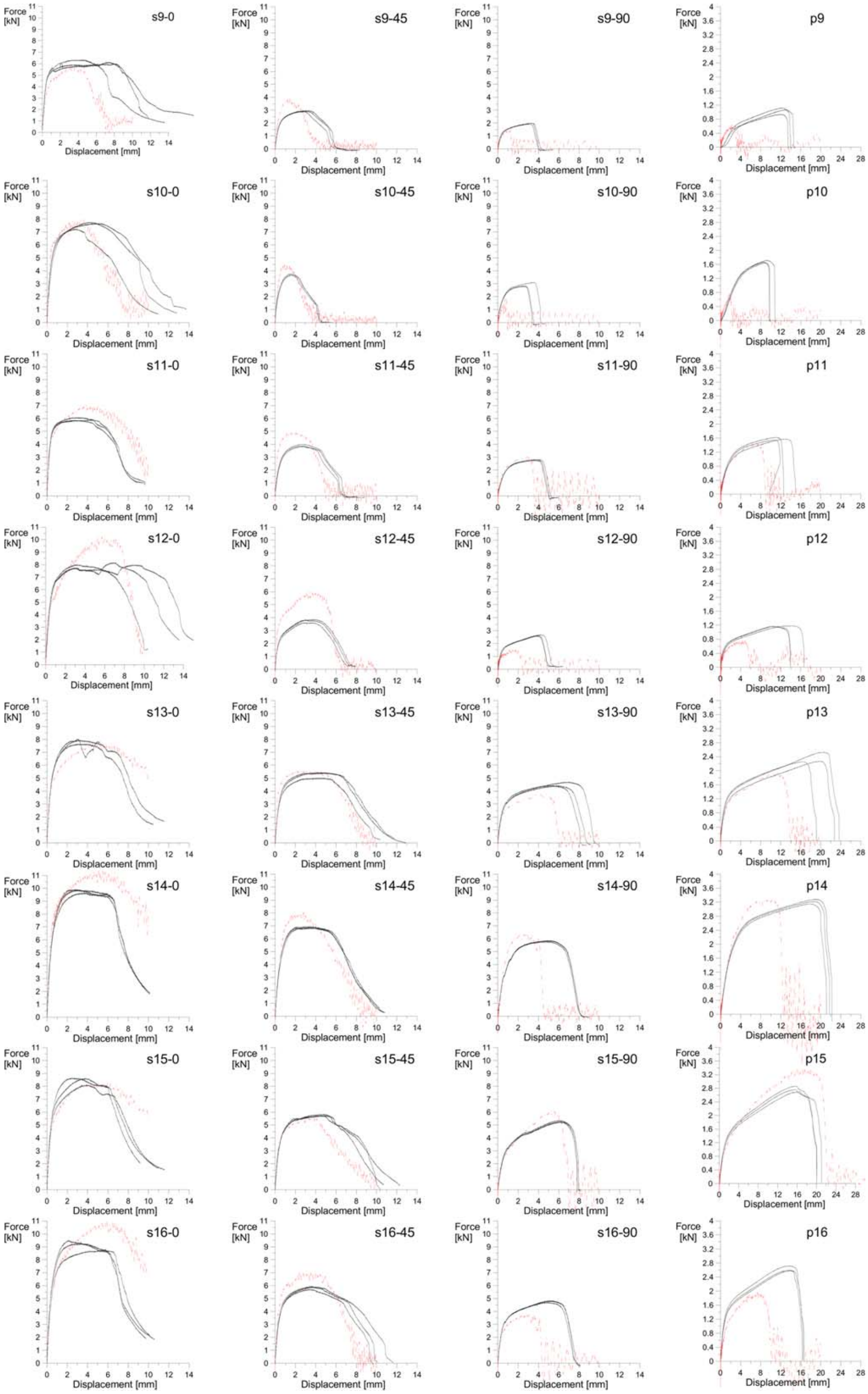

Fig. 25. Comparison between numerical and experimental force–displacement curves.

does not include any failure criterion for the material of the plates. In these cases, high plastic strains were detected in the region where failure was observed in the experiments. Differences between the numerical

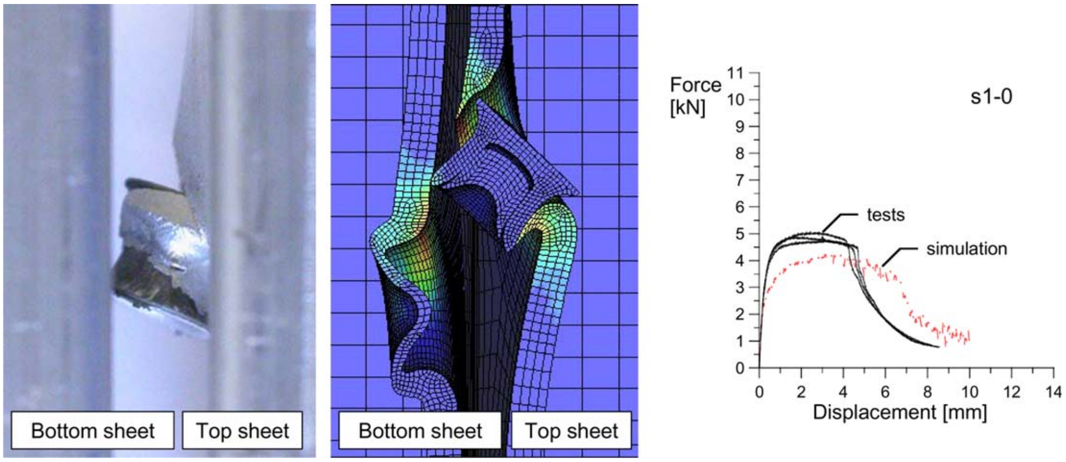

Fig. 26. Comparison between numerical and experimental failure modes for specimen s1 in pure shear condition.

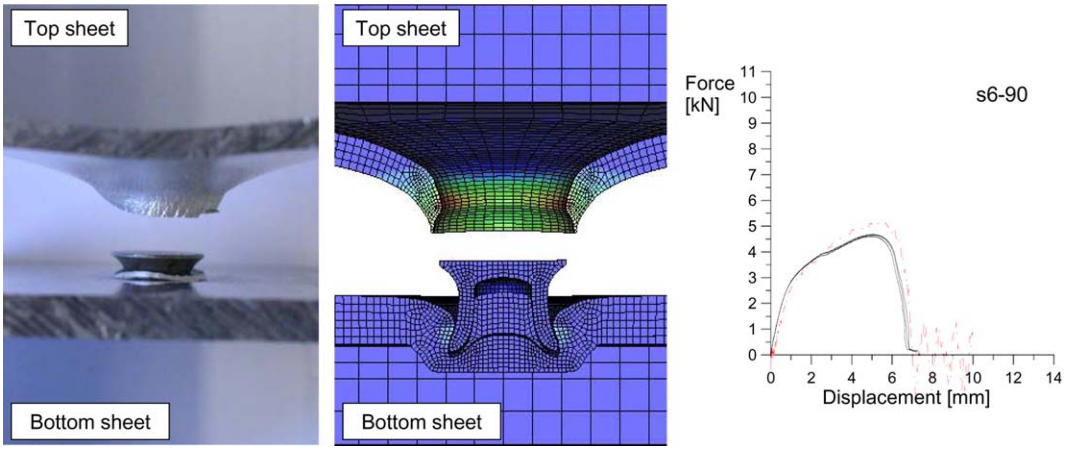

Fig. 27. Comparison between numerical and experimental failure modes for specimen s6 in pure pull-out condition.

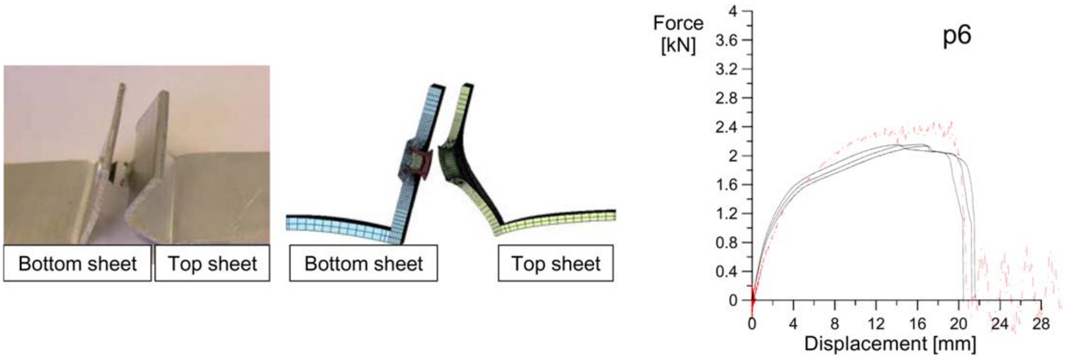

Fig. 28. Comparison between numerical and experimental failure modes for peeling specimen p6.

and experimental curves can also be explained by the variation in material properties for the base material, while in the numerical simulations no such variations have been considered. Fig. 26 shows a comparison between numerical and experimental failure modes for specimen s1 in a pure shear condition. The model is able to reproduce failure mode Fs1 with reasonable accuracy considering that no failure was defined in the material model of the plates. The rivet rotates and goes out from the bottom plate remaining partially stuck in the top plate. Fig. 27 shows a comparison between the numerical and the experimental failure modes for specimen s6 in the pure pull-out condition. Good agreement was observed in terms of failure mode that corresponds to a good agreement also for the force deformation curves. Finally, failure modes for the peeling specimen p6 are shown in Fig. 28. Good agreement was observed in terms of failure mode that corresponds to a good agreement also for the force deformation curves.

9. Conclusions

The behaviour of self-piercing riveted connections was investigated in this paper. An extensive experimental programme was conducted using aluminium alloy AA6060 in two different tempers, T4 and T6. Two different specimen geometries were used in this investigation: a U-shaped specimen and a peeling specimen. The experimental programme was focused on the influence of important model parameters such as thickness of the plates, geometry of the specimens, material properties of the plates and loading conditions. The influence of such parameter on the response of the connection was presented in term of force–displacement curves and failure modes. The experimental results were used to validate the 3D numerical model of the connection. The 3D FE representation of this connection was generated using the commercial code LS-DYNA. The model was based on the results obtained from the simulation of the riveting process. A new algorithm was generated in order to map the results from the 2D numerical model of the riveting process to the 3D numerical model of the connection. In this way, the simulation of the mechanical strength of the riveted joints was initialized with the proper deformed shape and the current post-riveting stress–strain state. The correct initialization of the model was important in order to obtain the correct force level in the simulation. First, the model was calibrated against one specimen configuration under two loading conditions, i.e. pure shear and pure pull-out. The influence of important parameters, i.e. the integration time, element formulation, contact formulation and mesh distribution, was studied. Then, the influence of the post-riveting stress–strain state on the mechanical properties of the rivet joint was studied. The model has shown that in order to get the correct force level it is necessary to include the stress–strain distribution from the riveting process. Second, the model was validated against experimental results. The model is able to reproduce the correct behaviour of the connection with reasonable accuracy, both in terms of the force–displacement curve and the deformation mode. For some configurations it was observed that for the pure pull-out condition, the model was not able to reproduce the correct force–displacement curve, due to a lack of penetration of the rivet shank in the bottom plate. Even so, the model was able to correctly predict the behaviour of those configurations under the pure shear condition. The model seems to be more sensitive for the pull-out condition than for the shear condition. The model was able to reproduce the correct failure mode for most of the specimens, but could not predict the failure modes related to failure in the base material since material failure was not included in the model. The model can be used to fully understand the behaviour of the connection, i.e. opening of the plates, rotation of the rivet at failure and forces acting on the rivet. All these information can be used to create a new shell-based rivet model for large-scale crash analysis of car structure.

Acknowledgements

The authors would like to acknowledge Hydro Aluminium, BMW and the Research Council of Norway for their support through the Norlight project.

References

Di Lorenzo, G., Landolfo, R., 2004. Shear experimental response of new connecting systems for cold-formed structures. Journal of Constructional Steel Research 60 (3–5), 561–579.

Fu, M., Mallick, P.K., 2001. Effect of process variables on the static and fatigue properties of self-piercing riveted joints in aluminium alloy5754. Society of Automotive Engineers, SAE Paper No. 2001-01-0825.

Hallquist, J.O., 1998. Theoretical Manual (compiled by J.O. Hallquist), Livermore Software Technology Corporation.

Lennon, R., Pedreschi, R., Sinha, B.P., 1999. Comparative study of some mechanical connections in cold formed steel. Construction and Building Materials 13 (3), 109–116.

Livermore Software, 2003. LS-DYNA Keyword Users Manual, version 970, Livermore Software Technology.

Porcaro, R., Hanssen, A.G., Aalberg, A., Langseth, M., 2004. Joining of aluminium using self-piercing riveting: testing, modelling and analysis. International Journal of Crashworthiness 9 (2), 141–154.

Porcaro, R., Hanssen, A.G., Langseth, M., Aalberg, A., in press. Self-piercing riveting process, an experimental and numerical investigation. Journal of Materials Processing Technology.